Electronic Supplementary Information for

The Role of the Iodine-atom Adduct in the Synthesis and Kinetics of Methyl Vinyl Ketone Oxide

— a Resonance-stabilized Criegee Intermediate

Yen-Hsiu Lin,[a,b] Yu-Lin Li,[a,b] Wen Chao,[a] Kaito Takahashi[a] and Jim Jr-Min Lin[a,b]*

[a]Institute of Atomic and Molecular Sciences, Academia Sinica, Taipei 10617, Taiwan

[b]Department of Chemistry, National Taiwan University, Taipei 10617, Taiwan.

*Corresponding Author: E-mail: jimlin@gate.sinica.edu.tw

ORCID:

Wen Chao: 0000-0003-0602-1606

Kaito Takahashi: 0000-0003-2339-4295

Jim Jr-Min Lin: 0000-0002-8308-2552

In this work, all the total pressures are N_2 gas balanced. The $Abs_{\text{precursor}}$ means the estimated peak absorbance of 1,3-diiodo-but-2-ene at 238.5 nm in the photolysis reactor (using $L \approx 6 \times 71$ cm = 426 cm). The absolute concentration of the precursor was not derived due to lack of its absolute cross section.

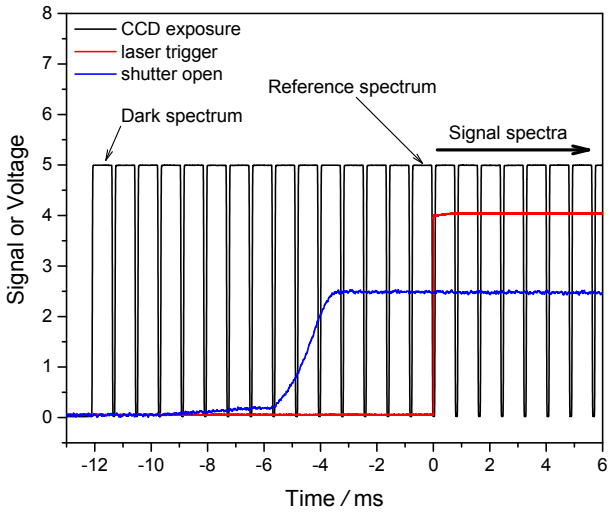

Figure S1. Example of the spectrum acquisition sequences. The black line shows the exposure time of EMCCD. The blue line shows the opening of the shutter (the signal of the probed light detected by a photodiode detector). The red line shows the trigger of the photolysis laser.

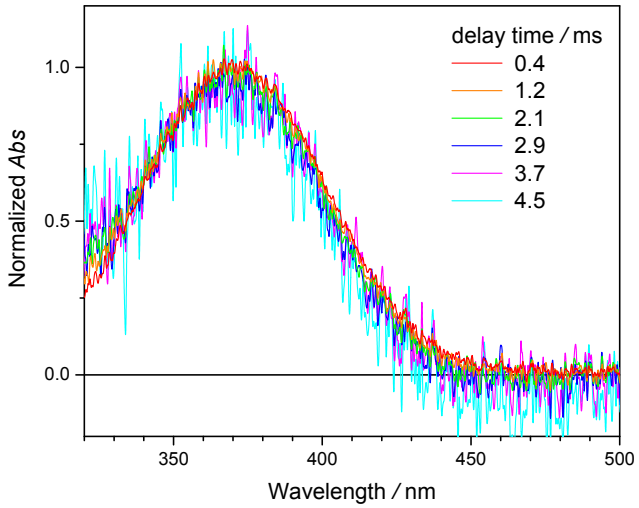

Figure S2. Height-normalized spectra (Exp S1a) recorded at different delay times (0.4, 1.2, 2.1, 2.9, 3.7, 4.5 ms). Minor contributions of the residue IO have been removed by subtracting scaled literature IO spectrum until the IO spectral peaks disappear.

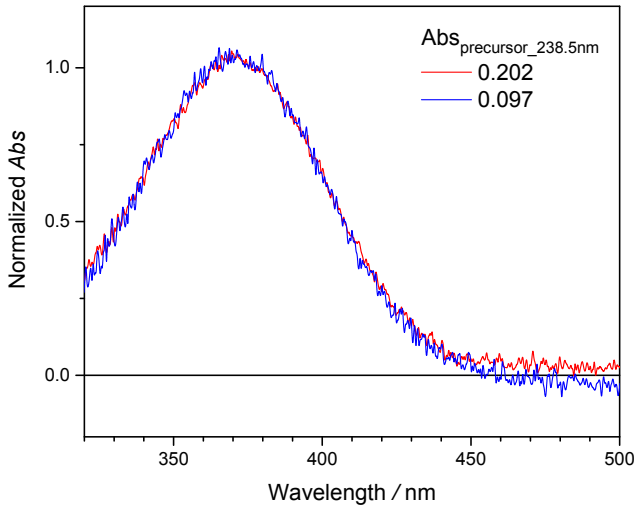

Figure S3. Height-normalized spectra at high and low precursor concentrations.
Each spectrum shows the average of the spectra recorded at 0.4, 1.2, 2.1 ms. Minor contributions of the residue IO have been removed by subtracting scaled literature IO spectrum until the IO spectral peaks disappear. The data are from Exp S2a and S3a.

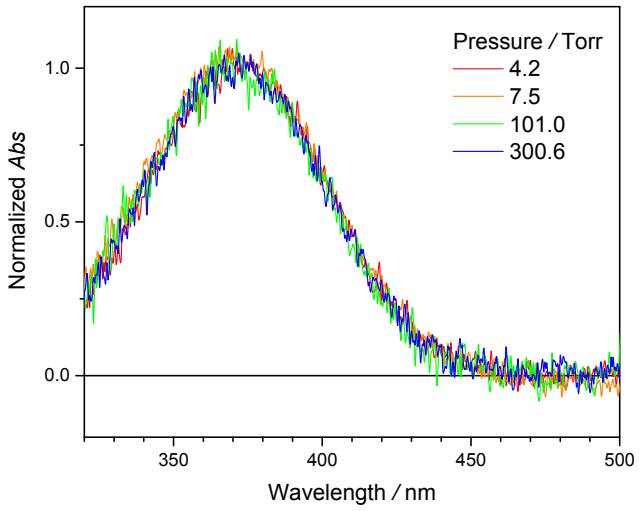

Figure S4. Height-normalized spectra at different total pressures.
The spectrum was measured at 4.2, 7.5, 101.0 and 300.6 Torr. Each spectrum shows the average of the spectra recorded at 0.4, 1.2, 2.1 ms. Minor contributions of the residue IO have been removed by subtracting scaled literature IO spectrum until the IO spectral peaks disappear. The data are from Exp S3a, S4e, S7a and S8a.

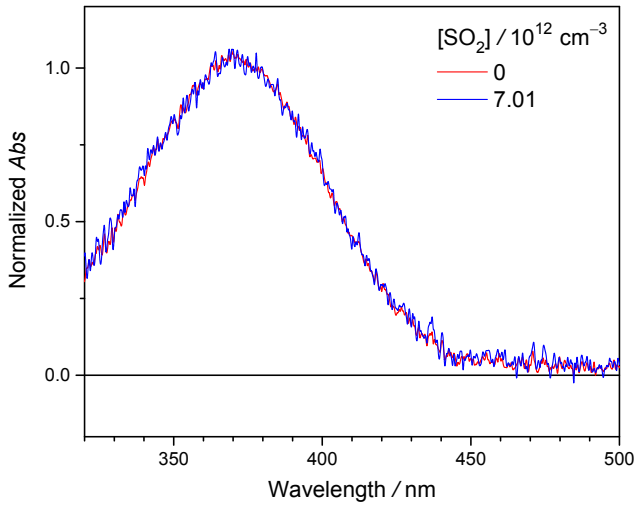

Figure S5. Height-normalized spectra at different [SO_2]. Each spectrum shows the average of the spectra recorded at 0.4, 1.2, 2.1 ms. Minor contributions of the residue IO have been removed by subtracting scaled literature IO spectrum until the IO spectral peaks disappear. The data are from Exp S2a and S2b.

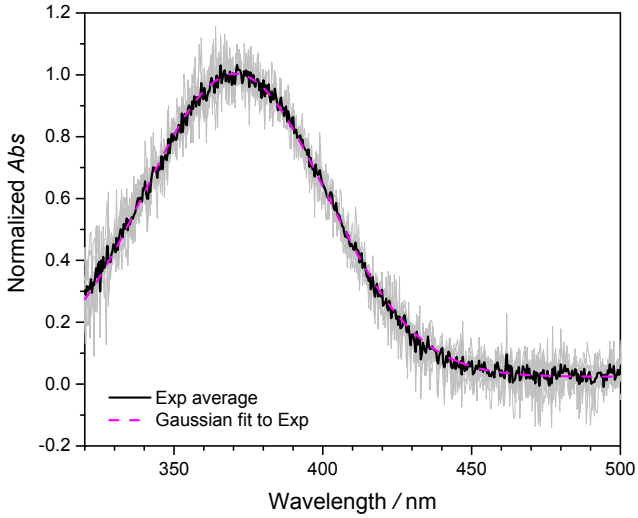

Figure S6. Height-normalized spectra of MVKO recorded at different experimental conditions, including delay times (0.4, 1.2, 2.0 ms), concentrations of the precursor (up to a factor of 6), and total pressures (101.0 and 300.6 Torr). Minor contributions of the residue IO have been removed by subtracting scaled literature IO spectrum until the IO spectral peaks disappear. A total of 8 selected spectra (choosing the ones with good S/N) are plotted as gray lines and their average is shown as black line. The latter is fitted with a Gaussian function (magenta dashed line, center 370.5 nm, FWHM 71.9 nm), similar to the spectrum reported by Caravan et al. which was recorded at a lower pressure of 7.4 Torr. The spectra are from Exp S6a, S7a, S8a, S9a, see Table S1 for the experimental conditions.

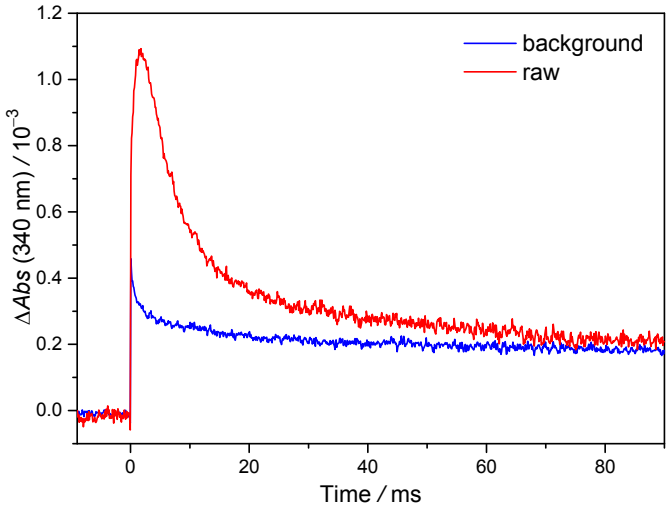

Figure S7. Time traces of the raw MVKO signal and background. The probe wavelength is 340±5 nm. The time zero is when the photolysis laser was fired. The data are from Exp K6a, Table 1.

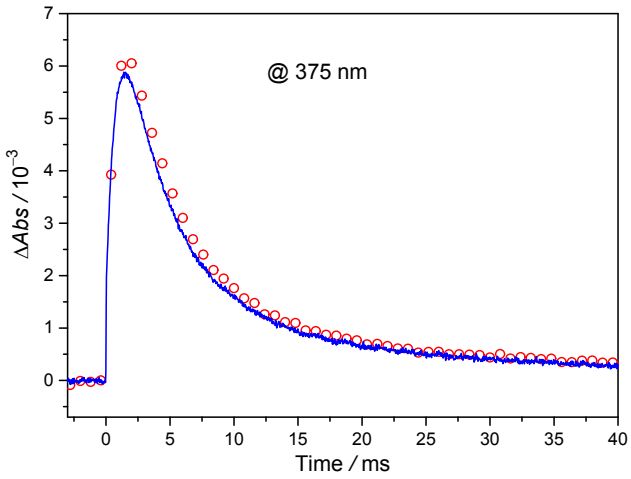

Figure S8. Blue line: typical time trace of MVKO absorption signal recorded at 300 Torr (with bandpass filter of 370–380 nm and balanced photodiode detector). Red circle: the MVKO absorption signal intensity (averaged value for 370–380 nm) obtained from the spectrum (EMCCD) measurements (part of the spectra are shown in Figure 4) under a similar condition (T = 298.5 K, laser fluence = 1.06 mJ cm^{-2}, $Abs_{\text{precursor}}$ = 0.35 and P_{O2} = 11.2/11.0 Torr for trace/spectrum). These two sets of data were acquired about 2 hours apart. The signal intensities are directly from the data (not scaled).

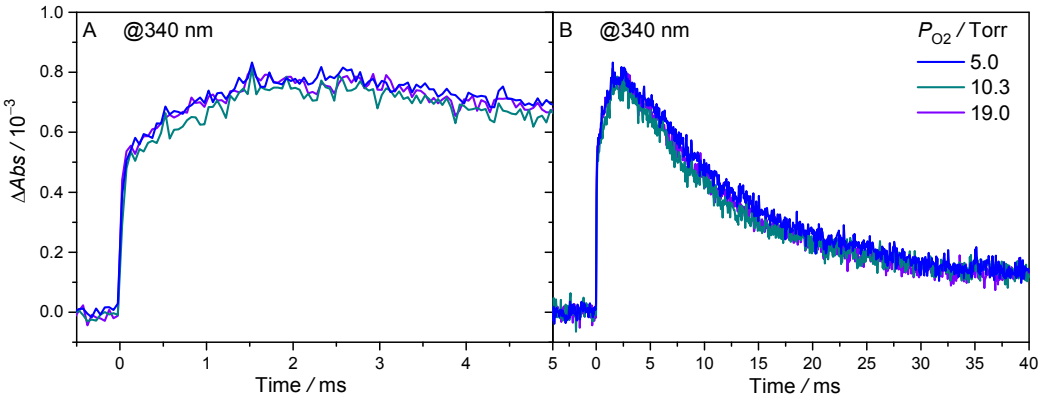

Figure S9. Time traces of the absorbance change of the 1,3-diiodo-but-2-ene/O_2 photolysis system at T = 299 K, P = 20 Torr, $Abs_{precursor}$ = 0.07, and different [O_2]. (dark cyan / blue / violet: 1.62 / 3.24 / 6.16 x 10^{17} cm^{-3}) The photolysis laser pulse sets the time zero. The laser pulse fluence is 1.02 mJ cm^{-2}.

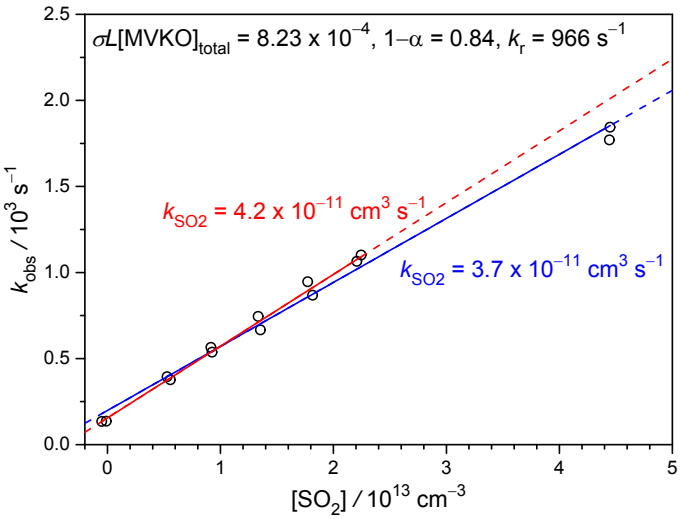

Figure S10. Plot of the local-fitted k_{obs} against [SO_2] (Exp K8a, except the data at the highest two [SO_2]). In the fitting of the time traces, σL[MVKO]$_{total}$, 1−α, and k_r are global parameters while k_{obs} and C_0 are local parameters. The solid parts of the lines in the figure indicate the selected ranges of the linear fitting to get k_{SO2}. Under high [SO_2] (> 2.5x10^{13} cm^{-3}), the MVKO signals are rather weak (see Figure 5), resulting in larger uncertainty of k_{SO2}. For [SO_2] < 2.5x10^{13} cm^{-3}, the fitting (red line) is more reliable and gives results similar to those from the global fitting (k_{SO2} = 4.24 x 10^{-11} cm^3 s^{-1}).

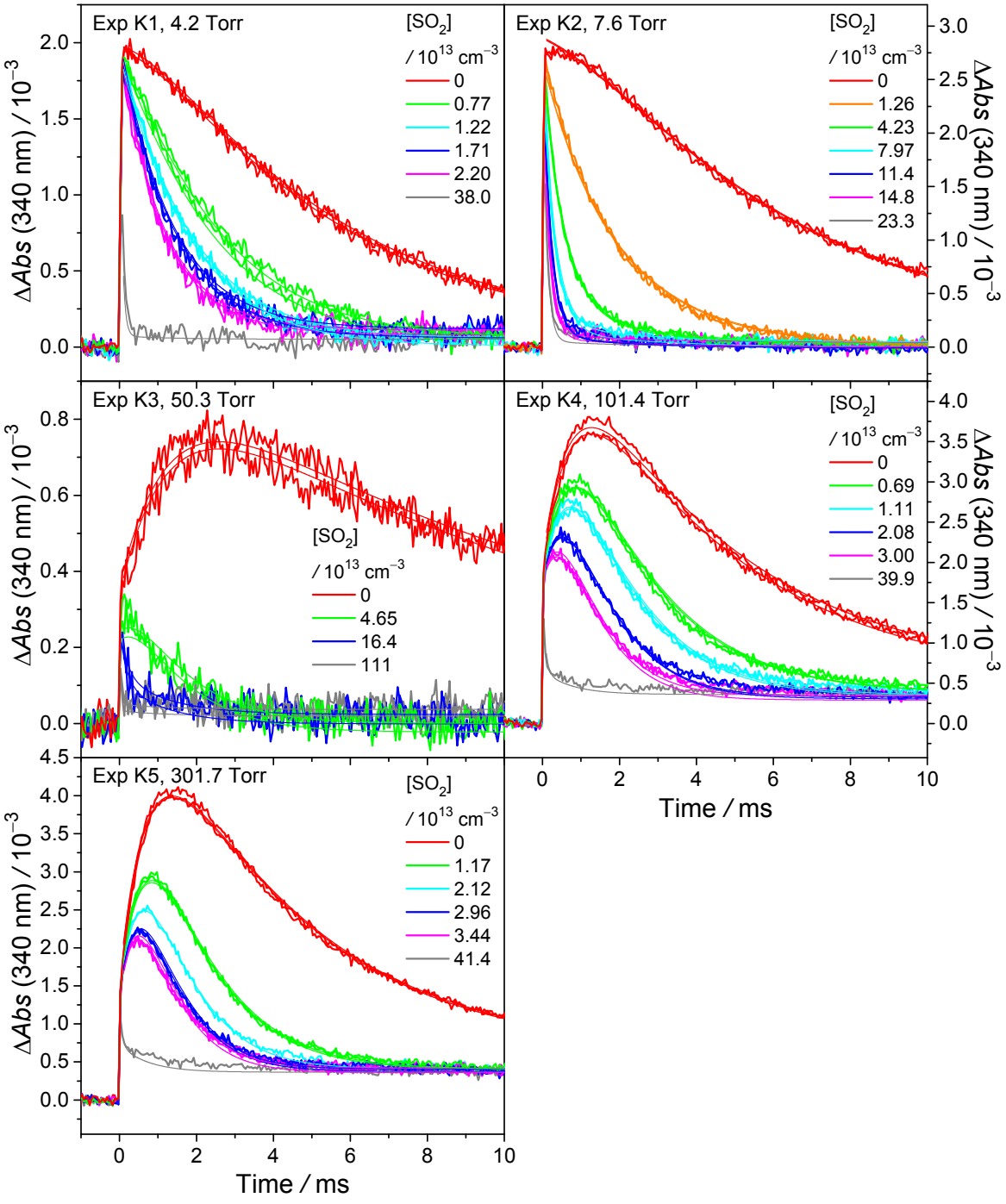

Figure S11. Typical time traces of the absorbance change at various [SO_2] and total pressure (4–302 Torr). The probe wavelength is 340±5 nm. The photolysis laser pulse sets the time zero. Smooth curves are the fitting results. The data are from Exp K1-K5.

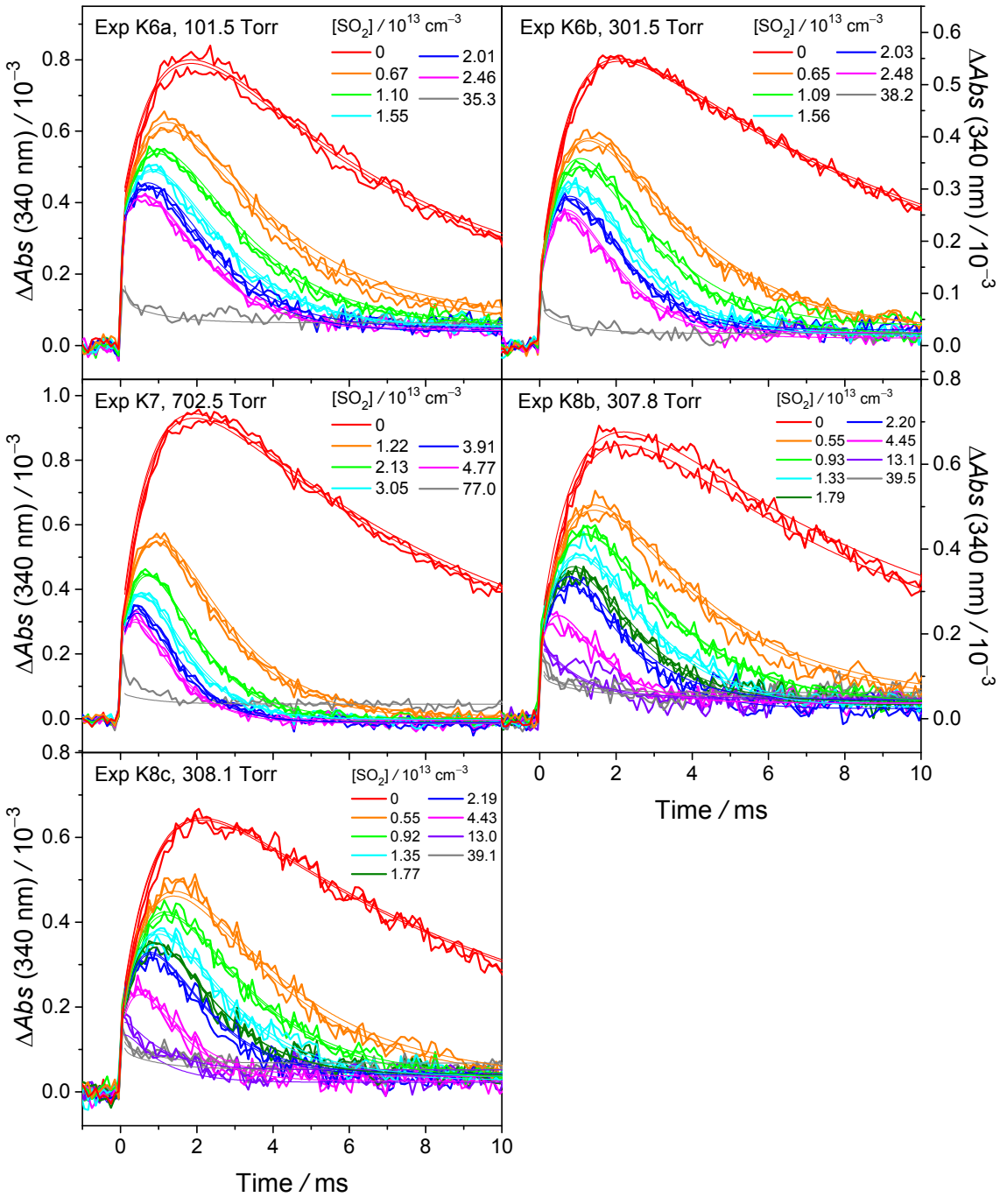

Figure S12. Typical time traces of the absorbance change at various [SO_2] and total pressure (102–703 Torr). The probe wavelength is 340±5 nm. The photolysis laser pulse sets the time zero. Smooth curves are the fitting results. The data are from Exp K6-K8.

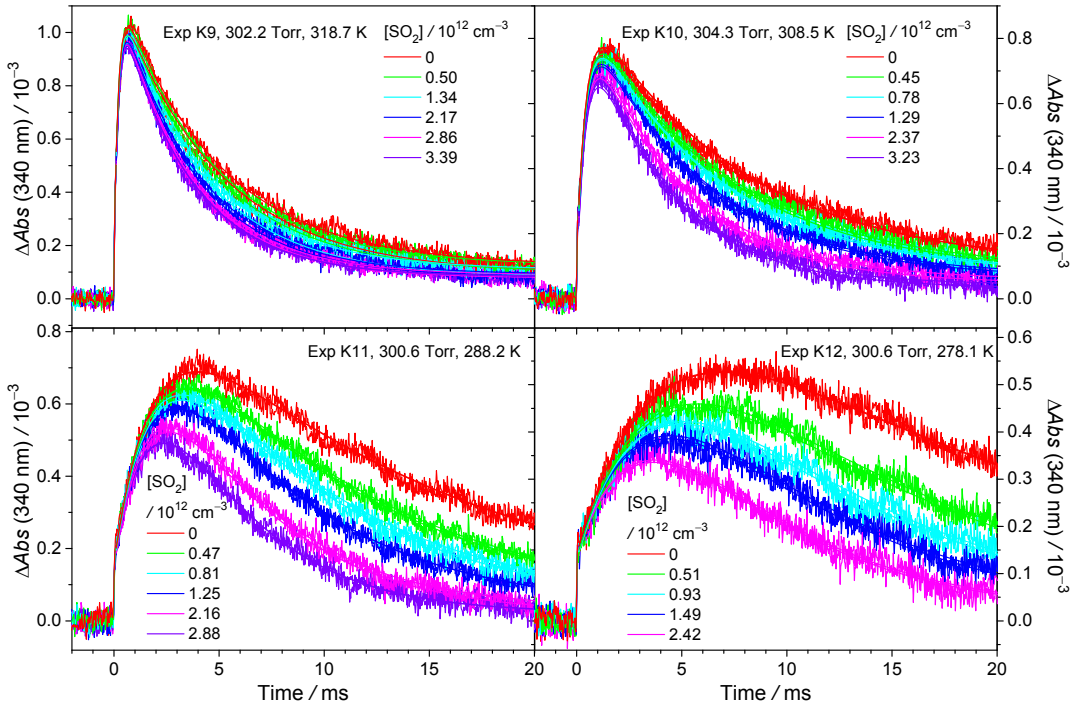

Figure S13. Time traces of the absorbance change of MVKO under various [SO_2] at 302 Torr and 278–319 K. The data are from Exp K9-K12.

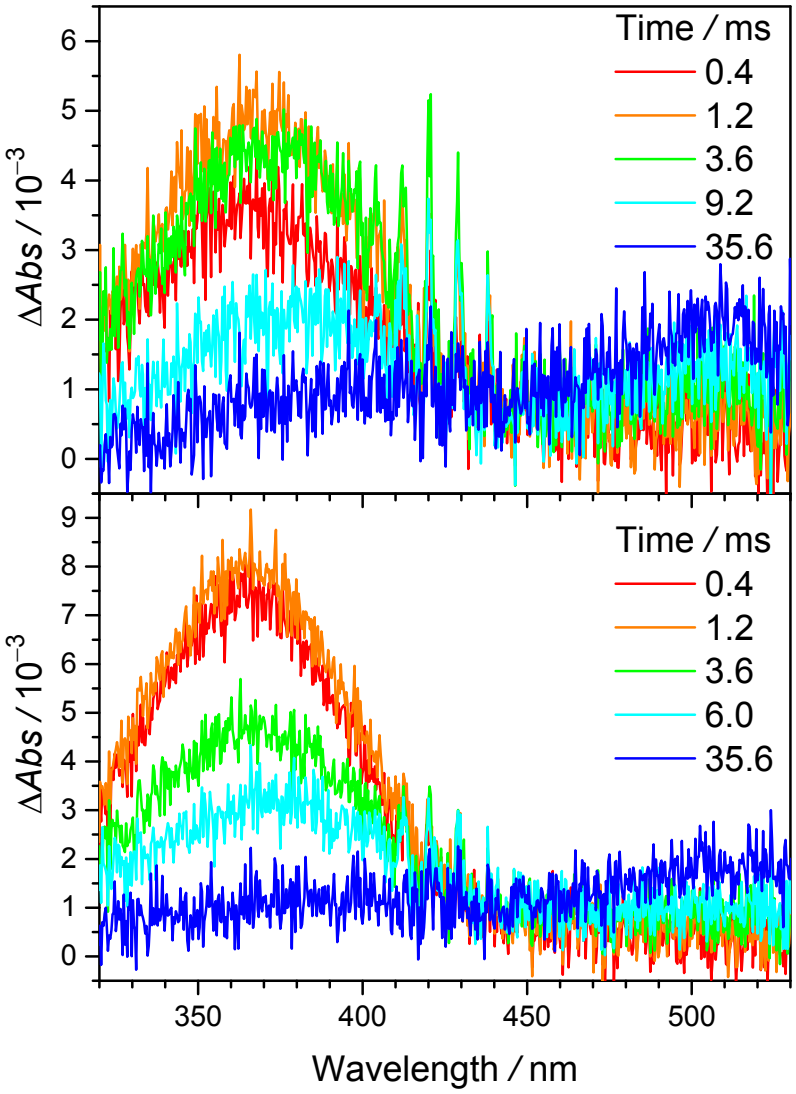

Figure S14. Difference absorption spectra of the 1,3-diiodo-but-2-ene/O_2 photolysis system recorded at selected delay times after the photolysis laser pulse under 300 Torr and 278 K (upper panel) / 319 K (lower panel). P_{O2} = 11 Torr; Laser fluence = 1.17 mJ cm^{-2} ; $Abs_{precursor}$ = 0.474 (upper panel) or 0.344 (lower panel). The relative contributions of the IO and I_2 byproducts are higher and the MVKO signal rises slower for the upper penal experiment. No other differences in the MVKO spectra are noticeable.

Table S1. Summary of experimental conditions for spectrum measurements at T = 297.2–299.5 K.

Exp. #.	$P_{reactor}$ / Torr	P_{O2} / Torr	$Abs_{precursor}$	[SO_2] / 10^{13} cm^{-3}
S1a	7.4	7.4	0.214	0
S1b	7.4	7.4	0.227	0
S1c	7.4	7.4	0.242	2.2
S1d	7.4	7.4	0.218	2.7
S1e	7.8	6.9	0.210	101.2
S1f	7.8	6.9	0.214	101.2
S2a	7.6	7.6	0.202	0
S2b	7.6	6.9	0.184	0.7
S2c	7.8	6.8	0.186	22.0
S3a	7.5	6.8	0.097	0
S3b	7.5	6.8	0.098	0.7
S3c	7.8	6.8	0.105	21.9
S4a	4.1	4.1	0.059	0
S4b	4.2	4.1	0.059	0.8
S4c	4.4	3.8	0.056	38.7
S4d	4.1	4.1	0.059	0.8
S4e	4.2	4.1	0.061	0
S5a	4.2	4.1	0.029	0
S5b	4.2	4.1	0.028	0.7
S5c	4.4	3.8	0.028	38.0
S5d	4.2	4.1	0.029	0.8
S5e	4.2	4.1	0.031	0
S6a	101.3	82.94	0.505	0
S6b	101.3	82.93	0.498	0.7
S6c	101.9	82.94	0.490	36.3
S7a	101.0	68.03	0.091	0
S7b	101.0	68.02	0.103	0.8
S7c	101.4	67.90	0.098	39.1
S8a	300.6	66.83	0.104	0
S8b	300.6	66.83	0.106	1.2
S8c	301.1	66.81	0.104	41.7
S9a	300.6	81.72	0.660	0
S9b	301.0	81.82	0.660	1.3
S9c	301.4	81.78	0.530	42.0

* The fluence of the laser pulse was 5.89 mJ cm^{-2}.

Computational Details

To understand the difference in the formation processes of CH_2OO and MVKO, we have calculated the stationary points for the precursor radicals (CH_2I and $CH_3(C_2H_3)CI$), adduct (CH_2IOO and $CH_3(C_2H_3)CIOO$), as well as the respective Criegee intermediate products using the B2PLYP[1] method using Dunning's cc-pVTZ basis set[2] for C, H and O while the pseudopotential based cc-pVTZ-PP[3] was used for the I atom. Throughout the paper we will use the symbol "VTZ" to describe this basis set. The empirical dispersion correction was added in using Grimme's D3 method with Becke-Johnson damping (D3BJ).[4] The oxygen molecule was optimized at the triplet ground electronic state, while the precursor radical, adduct, and iodine atom were optimized at the doublet ground electronic state, and the Criegee intermediates were optimized at the singlet ground electronic state. Using the obtained optimized geometries, we have performed energy correction using the explicitly correlated coupled cluster singles and doubles with perturbative triples, CCSD(T)-F12b method[5] with the cc-pVTZ-F12 basis sets for C, H, O and the cc-pVTZ-PP-F12 for I.[6,7] For the CH_2IOO system, we also performed the CCSD(T)-F12 calculations using the bigger cc-pVQZ-F12, and cc-pVQZ-F12-PP basis sets to evaluate the convergence of the obtained energies with respect to the basis sets. For the $CH_2I + O_2 \rightarrow CH_2IOO$ channel, the adduct binding energy given by the VQZ-F12 basis is 26.7 kcal mol^{-1}, 0.3 kcal mol^{-1} larger than the VTZ-F12 result; while for the $CH_2OO + I \rightarrow CH_2IOO$ channel, it is 26.4 kcal mol^{-1}, smaller than the VTZ-F12 result by 0.9 kcal mol^{-1}. The error of using the VTZ-F12 energies instead of the ones at the complete basis set limit may give an order of magnitude error in the calculated equilibrium constants. The energy of the iodine atom was corrected for spin-orbit coupling using the recommended value of 7.24 kcal mol^{-1}, given in the Computational Chemistry Comparison and Benchmark DataBase.[8]

In addition, to understand the adduct formation process $CH_2I+O_2 \rightarrow CH_2IOO$ ($CH_3(C_2H_3)CI+O_2 \rightarrow CH_3(C_2H_3)CIOO$) as well as the Criegee intermediate formation from the adduct $CH_2IOO \rightarrow CH_2OO+I$ ($CH_3(C_2H_3)CIOO \rightarrow CH_3(C_2H_3)COO+I$), we calculated the partially optimized potential energy curve along the C–I bond length as well as the C–O bond length. Following previous studies,[9] we tested several different methods B2PLYP-D3BJ, B3LYP, and B3LYP-D3BJ. For B2PLYP-D3BJ we encountered bad convergence at long bond lengths, R_{CI} greater than 3.5 Å, so we will present the results for B3LYP-D3BJ in the figure below. We note that at shorter bond lengths, the trends for all three density functional theory methods are very similar. As seen in Figure S15, the biggest difference between the CH_2OO and MVKO is in the binding energies of the adducts. We believe that the energy barrier seen for the MVKO channel along the CO bond

dissociation is due to the use of single reference method. Indeed, Klippenstein and coworkers[10] have shown that using multireference methods, the dissociation curve will not have a barrier. More elaborate calculation using the variational transition state approach with potential energy curves obtained using multireference methods including spin-orbit coupling will be required to obtain rate coefficients for the formation process, but it is beyond the scope of the present research. We also note that due to the existence of numerous rotational conformers for MVKO and its precursor as well as the adduct, accurate values for the equilibrium constant will require hindered rotor treatment including all the conformers. In the present study, we only considered the most stable conformations with rigid rotor harmonic oscillator approximation, and this will lead to some uncertainties. However, we believe the main difference in the equilibrium constant between MVKO versus CH_2OO is attributed to the large difference in the relative energies of the adducts.

All B2PYP-D3BJ, B3LYP-D3BJ and B3LYP calculations were performed by Gaussian16 program,[11] and the CCSD(T)-F12b calculations were performed by the MOLPRO2019 program.[12]

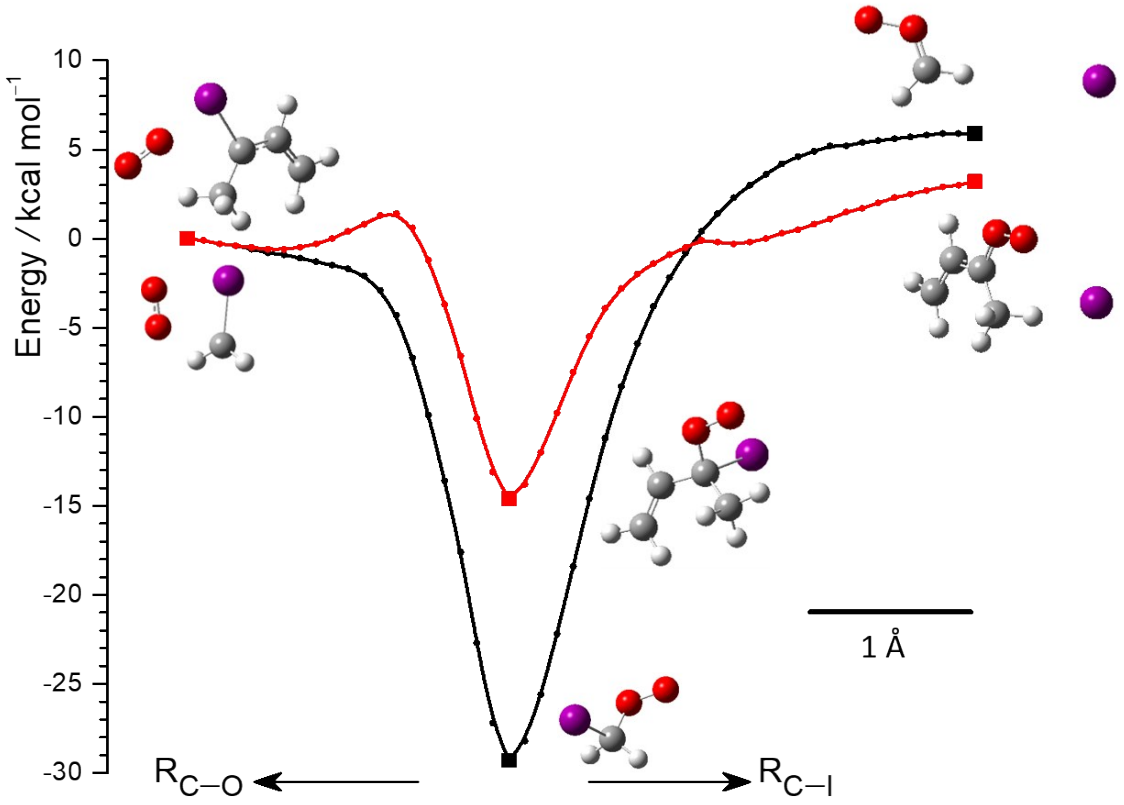

Figure S15. The effective potential energy curve, calculated by B3LYP-D3BJ/VTZ, along the C–I and C–O bonds for the CH_2OO + I (black) and MVKO + I (red) systems. The zero of the energy is taken at CH_2I+O_2 and $CH_3(C_2H_3)CI+O_2$, respectively. The corresponding energies of the plotted geometries are shown as square symbol. As mentioned above, the energy barrier seen for the $CH_3(C_2H_3)CI+O_2$ channel is probably an artifact due to the use of single reference method. In this plot, we did not add in the spin-orbit correction for the iodine atom, such that the energies at long C–I distances are over estimated.

Comparison between the adduct yields in the CH_2IOO and $CH_3(C_2H_3)CIOO$ systems

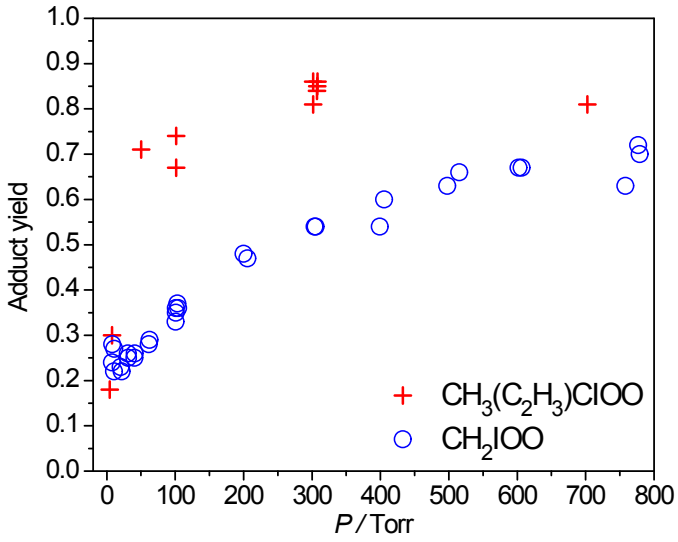

Figure S16. The yields of the adducts as functions of the total pressure (N_2/O_2) in the CH_2IOO (from Ting et al.[13]) and $CH_3(C_2H_3)CIOO$ (this work) systems. The latter one shows a lower pressure onset for the saturation in the adduct yield. There may be multiple explanations for this observation. A possible reason is the following. The $CH_3(C_2H_3)CIOO$ system has much larger vibrational degrees of freedom, which buffer the excess energy and thus lengthen the lifetime of the collisional complex. As a result, the effective probability of collisional relaxation is higher.

References:

1. S. Grimme, J. Chem. Phys., 2006, 124, 034108.
2. T.H. Dunning, Jr. J. Chem. Phys. 1989, 90, 1007.
3. K.A. Peterson, B.C. Shepler, D. Figgen and H. Stoll, J. Phys. Chem. A , 2006, 110, 13877.
4. S. Grimme, J. Antony, S. Ehrlich and H. Krieg, J. Chem. Phys., 2010, 132, 154104
5. G. Knizia, T. B. Adler, and H.-J. Werner, J. Chem. Phys. 2009, 130, 054104.
6. K. A. Peterson, J. Chem. Phys. 2008, 128, 084102.
7. J G Hilll and K. A. Peterson, J. Chem. Phys. 2014, 141, 094106.
8. https://cccbdb.nist.gov/elecspin.asp, last visited 3/25/2020.
9. Y. Su el al. Nat Chem, 2014, 6, 477.
10. V. P. Barber et al. J. Am. Chem. Soc., 2018, 140, 10866.
11. Gaussian 16, Revision A.03, M. J. Frisch, G. W. Trucks, H. B. Schlegel, G. E. Scuseria, M. A. Robb, J. R. Cheeseman, G. Scalmani, V. Barone, G. A. Petersson, H. Nakatsuji, X. Li, M. Caricato, A. V. Marenich, J. Bloino, B. G. Janesko, R. Gomperts, B. Mennucci, H. P. Hratchian, J. V. Ortiz, A. F. Izmaylov, J. L. Sonnenberg, D. Williams-Young, F. Ding, F. Lipparini, F. Egidi, J. Goings, B. Peng, A. Petrone, T. Henderson, D. Ranasinghe, V. G.

Zakrzewski, J. Gao, N. Rega, G. Zheng, W. Liang, M. Hada, M. Ehara, K. Toyota, R. Fukuda, J. Hasegawa, M. Ishida, T. Nakajima, Y. Honda, O. Kitao, H. Nakai, T. Vreven, K. Throssell, J. A. Montgomery, Jr., J. E. Peralta, F. Ogliaro, M. J. Bearpark, J. J. Heyd, E. N. Brothers, K. N. Kudin, V. N. Staroverov, T. A. Keith, R. Kobayashi, J. Normand, K. Raghavachari, A. P. Rendell, J. C. Burant, S. S. Iyengar, J. Tomasi, M. Cossi, J. M. Millam, M. Klene, C. Adamo, R. Cammi, J. W. Ochterski, R. L. Martin, K. Morokuma, O. Farkas, J. B. Foresman, and D. J. Fox, Gaussian, Inc., Wallingford CT, 2016.

12. MOLPRO, version 2019.2, a package of ab initio programs, H.-J. Werner, P. J. Knowles, G. Knizia, F. R. Manby, M. Schütz, P. Celani, W. Györffy, D. Kats, T. Korona, R. Lindh, A. Mitrushenkov, G. Rauhut, K. R. Shamasundar, T. B. Adler, R. D. Amos, S. J. Bennie, A. Bernhardsson, A. Berning, D. L. Cooper, M. J. O. Deegan, A. J. Dobbyn, F. Eckert, E. Goll, C. Hampel, A. Hesselmann, G. Hetzer, T. Hrenar, G. Jansen, C. Köppl, S. J. R. Lee, Y. Liu, A. W. Lloyd, Q. Ma, R. A. Mata, A. J. May, S. J. McNicholas, W. Meyer, T. F. Miller III, M. E. Mura, A. Nicklass, D. P. O'Neill, P. Palmieri, D. Peng, K. Pflüger, R. Pitzer, M. Reiher, T. Shiozaki, H. Stoll, A. J. Stone, R. Tarroni, T. Thorsteinsson, M. Wang, and M. Welborn, , see https://www.molpro.net.
13. W. L. Ting, C. H. Chang, Y. F. Lee, H. Matsui, Y. P. Lee and J. J. Lin, J. Chem. Phys., 2014, 141, 104308.